

Soft X-ray Spectral Diagnostics of Multi-thermal Plasma in Solar Flares with Chandrayaan-2 XSM

N. P. S. MITHUN,^{1,2} SANTOSH V. VADAWALE,¹ GIULIO DEL ZANNA,³ YAMINI K. RAO,³ BHUWAN JOSHI,¹
AVEEK SARKAR,¹ BISWAJIT MONDAL,¹ P. JANARDHAN,¹ ANIL BHARDWAJ,¹ AND HELEN E. MASON³

¹*Physical Research Laboratory, Navrangpura, Ahmedabad, Gujarat-380 009, India*

²*Indian Institute of Technology Gandhinagar, Palaj, Gandhinagar, Gujarat-382 355, India*

³*DAMTP, Centre for Mathematical Sciences, University of Cambridge, Wilberforce Road, Cambridge, CB3 0WA, UK*

Submitted to ApJ

ABSTRACT

Spectroscopic observations in X-ray wavelengths provide excellent diagnostics of the temperature distribution in solar flare plasma. The Solar X-ray Monitor (XSM) onboard the Chandrayaan-2 mission provides broad-band disk integrated soft X-ray solar spectral measurements in the energy range of 1-15 keV with high spectral resolution and time cadence. In this study, we analyse X-ray spectra of three representative GOES C-class flares obtained with the XSM to investigate the evolution of various plasma parameters during the course of the flares. Using the soft X-ray spectra consisting of the continuum and well-resolved line complexes of major elements like Mg, Si, and Fe, we investigate the validity of the isothermal and multi-thermal assumptions on the high temperature components of the flaring plasma. We show that the soft X-ray spectra during the impulsive phase of the high intensity flares are inconsistent with isothermal models and are best fitted with double peaked differential emission measure distributions where the temperature of the hotter component rises faster than that of the cooler component. The two distinct temperature components observed in DEM models during the impulsive phase of the flares suggest the presence of the directly heated plasma in the corona and evaporated plasma from the chromospheric footpoints. We also find that the abundances of low FIP elements Mg, Si, and Fe reduces from near coronal to near photospheric values during the rising phase of the flare and recovers back to coronal values during decay phase, which is also consistent with the chromospheric evaporation scenario.

Keywords: Sun: X-rays – Sun: corona – Sun: Flares

1. INTRODUCTION

Solar flares are sudden releases of energy in the lower atmosphere of the Sun. They emit across the entire electromagnetic spectrum and are responsible for accelerating particles. Various observations point to magnetic reconnection as the underlying mechanism powering the flares, which accelerates the particles to high energies and heats the plasma to temperatures higher than a few million kelvin (Benz 2017). The standard flare model, also known as CSHKP model (Carmichael 1964; Sturrock 1966; Hirayama 1974; Kopp & Pneuman 1976), has been successful in explaining several observed features of solar flares. However, multiple aspects such as the exact location of particle acceleration and heating and the acceleration mechanism still remain unspecified (Benz 2017; Krucker et al. 2008). Resolving these issues requires knowledge of the local plasma's thermal and non-thermal particle distributions, which can be best obtained from the X-ray and EUV observations (Del Zanna & Mason 2018).

More often than not, flare thermal plasma is composed of particles at multiple temperatures. The differential emission measure (DEM) is a way to quantify the thermal plasma at different temperatures and densities along the line-of-sight. Ideal observations to required obtain the DEM in flaring regions would be spatially resolved measurements

of individual spectral lines of various elements formed at different temperatures. While there are concept designs of instruments that may be capable of such measurements (Laming et al. 2010; Matthews et al. 2021; Del Zanna et al. 2021a), there are currently no such instruments available.

However, it is possible to derive spatially resolved DEMs by using the multi-band images in EUV with the SDO AIA (Cheung et al. 2015; Su et al. 2018) or in X-rays with the Hinode XRT (Goryaev et al. 2010), both of which provide limited spectral information. In the case of AIA, even though the wavelength bands are relatively narrow, they include multiple spectral lines that are formed at different temperatures. In the case of XRT, in addition to lines formed at different temperatures, there is a significant contribution from the continuum which is strongly dependant on temperature. This results in broad temperature responses for different wavelength bands making it difficult to obtain unique DEM solutions.

Another approach is to use high resolution spectra in the EUV or X-rays, but without any spatial information, where individual lines formed at different temperatures are well resolved. Earlier observations with SMM/BCS, Yokoh/BCS, and other crystal spectrographs in X-ray wavelengths have provided evidence of multi-thermal plasma distributions (Doschek 1990; Feldman 1996). More recently, DEM distributions have been obtained with this approach using observations with SDO EVE (Warren et al. 2013) and RESIK (Sylwester et al. 2014; Kepa et al. 2018) observations. Observations in X-rays are more sensitive to hotter plasma ($\sim > 10$ MK) than EUV observations and thus combining both EUV and higher energy X-ray observations can be advantageous. For example, Caspi et al. (2014) and McTiernan et al. (2019) have carried out joint analyses of EUV spectra from EVE along with X-ray observations (> 3 keV) with RHESSI to obtain better constraints on the DEM. Similar studies have also been carried out recently with the FOXSI hard X-ray imaging telescope (Athiray et al. 2020). As observations in lower energy X-rays down to 1 keV complement the temperature ranges covered by EUV and X-ray observations at higher energies by RHESSI, there have also been attempts to use spatially and spectrally integrated soft X-ray measurements from GOES XRS along with EUV spectra to constrain the DEM (Warren 2014). The broadband counts from GOES, dominated by the continuum (Del Zanna & Woods 2013), provide limited temperature diagnostics in comparison to having the complete spectral data.

Spatially integrated, but spectrally resolved soft X-ray observations can provide better constraints to the DEM and complement EUV and hard X-ray observations. There have been a few instruments in the past such as SOXS (4 – 25 keV, Jain et al. 2005, SphinX (1 – 15 keV, Gburek et al. 2013), and MinXSS (1 – 15 keV, Moore et al. 2018) that have provided soft X-ray spectral measurements. Often soft X-ray spectra from these instruments are fitted with isothermal models; however, there have also been studies that have used X-ray spectral data to obtain the differential emission measure (Awasthi et al. 2016).

If the soft X-ray spectra have sufficient energy resolution to resolve the line complexes of individual elements, then it is also possible to constrain and measure the abundances of elements during the course of flares, self consistently with DEM. Recent reports of measurements of elemental abundances during flares obtained by isothermal fits to the soft X-ray spectra show close to photospheric abundances during the flare peaks (Mondal et al. 2021; Narendranath et al. 2020).

Here, we attempt to investigate the evolution of the temperature structure and elemental abundances during solar flares using soft X-ray observations with the Solar X-ray Monitor (XSM) on board the Chandrayaan-2 mission (Vadawale et al. 2014; Shanmugam et al. 2020; Mithun et al. 2020). The XSM provides disk-integrated spectral observations in the energy range of 1 – 15 keV with the highest energy resolution thus far for such broadband spectrometers. Soft X-ray spectra obtained with the XSM for sub-A class events have been shown to be consistent with an isothermal model (Vadawale et al. 2021). It is also observed that the spectra are well described with a single temperature plasma emission model during the evolution of B-class flares (Mondal et al. 2021). However, for more complex and larger flares such as C-class events, we explore here the validity of isothermal models in fitting the observed spectrum. We then propose a scheme for DEM analyses of X-ray spectra, such as that with the XSM, assuming simple functional forms for the DEM distribution. These methods are employed to obtain the evolution of the DEM during the course of the flare along with the evolution of abundances of some of the elements.

Section 2 provides details of the observations of the flares considered in the present work and the data reduction. Analysis of the spectra with an isothermal approximation is presented in Section 3 and Section 4 presents the analysis and results considering a multi-thermal plasma. Results are discussed and summarized in Section 5.

2. OBSERVATIONS OF FLARES WITH XSM AND DATA REDUCTION

The Chandrayaan-2 Solar X-ray Monitor (XSM) carries out Sun-as-a-star observations and measurements of the 1–15 keV X-ray spectra with an energy resolution of ~ 175 eV at 5.9 keV at one second cadence (Vadawale et al. 2014; Shanmugam et al. 2020; Mithun et al. 2020). The XSM has been observing the Sun since September 2019 and the solar X-ray light curves are available on the XSM website¹. As the visibility of the Sun for XSM varies with orbital seasons (Mithun et al. 2021a), there are long periods without solar observations. Also, with XSM being in a lunar orbit, there are periods when the Sun is occulted by the Moon, thereby resulting in partial observations of solar flares. For the present work, we selected three representative GOES C-class flares having 1–8 Å peak fluxes in ranging from 1.5×10^{-5} Wm⁻² to 8.5×10^{-5} Wm⁻², for which XSM observations are available for the entire flare duration. The selected flares are SOL-2020-10-16T12:57 (C1.57), SOL-2021-10-07T02:46 (C5.70), and SOL-2021-09-08T17:32 (C8.40)

For each of the flares, we generated X-ray light curves from XSM raw data using the `xsmgenlc` task from the XSM Data Analysis Software (Mithun et al. 2021b) with the default good time intervals. The light curves were generated in different energy bands at a cadence of 1 minute, after correcting for the instrument effective area variations with Sun angle over time. Figure 1 shows the XSM light curves in different energy bands for the three flares. For comparison, X-ray flux light curves from the GOES-16/17 XRS instrument in the 1–8 Å band are also shown in the figure.

It can be seen that all three flares follow the general characteristics, i.e. an impulsive phase and a gradual phase which lasts progressively longer for larger flares. Light curves in different energy bands follow the expected nature that the higher energy bands peak earlier compared to progressively lower energy bands. We also compute the derivative of the soft X-ray (1–15 keV) XSM light curve which is expected to be similar to the impulsive hard X-ray emission by the Neupert effect (Neupert 1968). We denote the peak of the flux derivative as the impulsive phase peak, marked by vertical dashed lines in the figure. Times corresponding to the peak count rate in 1–15 keV band are also shown in the figure with vertical dotted lines.

Further, to carry out a spectral analysis with XSM data, time resolved spectra are generated for one minute intervals using `xsmgenspec`. A one minute time bin was chosen to ensure that a sufficient number of counts are present in the spectra to carry out spectral fitting. For each spectrum, a corresponding ancillary response file with effective area was also generated. The spectra and response files are in standard formats that are compatible with the XSPEC spectral fitting package (Arnaud 1996) used for modeling the spectra. The default bin size for spectral channels is 33 eV. At higher energies, the counts in individual channels are low, so such channels were grouped together using the `grppha` task available as part of the HEASOFT distribution. For each spectrum, the 1.0–1.3 keV band where the instrument effective area is not well modelled (Mithun et al. 2020) is ignored in the analysis and the spectrum above 1.3 keV is fitted. Using the XSM observations when the Sun was out of its field of view, the non-solar background spectrum was generated and subtracted from the observed total spectrum during the flares. Solar spectra have significantly higher counts compared to the background at low energies, but not at high energies. Thus, at higher energies, spectral fitting is limited to the energy range where the observed counts are higher than the background counts. It may be noted that the energy range differs for each spectra depending on the solar flux.

3. ISOTHERMAL APPROXIMATION

Solar flare spectra in the soft X-ray band are often approximated with isothermal emission models with temperature, volume emission measure, and abundances of various species as parameters. It has been shown that the soft X-ray spectra of sub-A class flares observed by the XSM can be well described using isothermal models (Vadawale et al. 2021). Further, for all B-class events observed during the first two seasons, Mondal et al. (2021) have shown that the time-resolved spectra during the course of the flare are also consistent with isothermal models. Being the simplest model, we first analyze the spectra of the C-class flares considered for the present study using an isothermal approximation.

We use PyXSPEC², the python interface for XSPEC, for analysis of the time-resolved spectra generated for one-minute intervals as discussed in the previous section. The spectra are fitted with a model for isothermal emission computed using the CHIANTI atomic database version 10.0 (Del Zanna et al. 2021b). The spectral model `chisoth`³ is implemented as a local model in XSPEC and uses tabulated spectra computed using CHIANTI for each elemental species (up to Zn) over a grid of temperatures to obtain model spectra for any temperature, emission measure, and abundances, as described in Mondal et al. (2021). While fitting the flare spectra, abundances of all elements are initially set to coronal abundances from Feldman (1992). Then, for each spectrum, major elements whose line complexes are

¹ <https://www.prl.res.in/ch2xsm/>

² <https://heasarc.gsfc.nasa.gov/xanadu/xspec/python/html/index.html>

³ <https://github.com/xastprl/chspec>

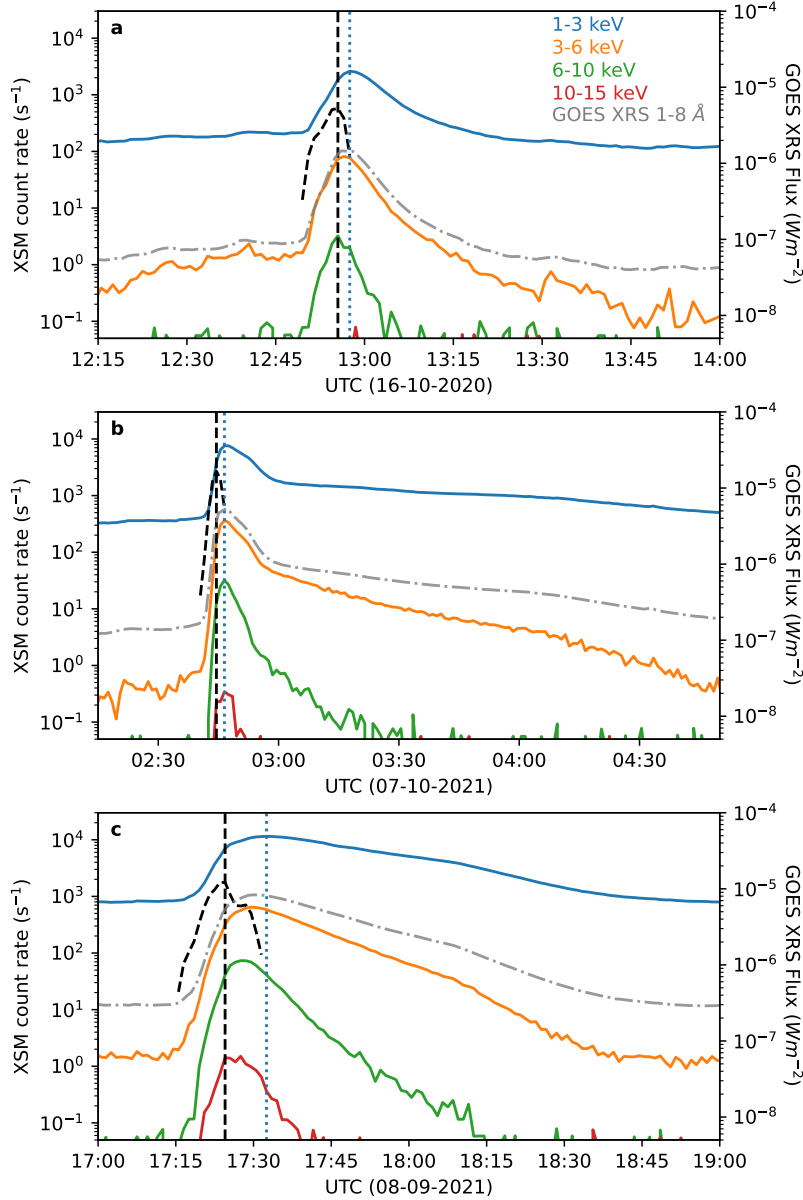


Figure 1. XSM light curves in different energy bands for the three C-class flares on 16-Oct-2020 (a), 07-Oct-2021 (b), and 08-Sep-2021 (c). GOES XRS 1-8 Å band flux is shown in grey. All light curves are at one minute cadence. The y-range is selected such that the points shown have at least 2 sigma detection. The derivative of the XSM 1–15 keV count rate is shown with a black dashed line and the vertical black dashed line denotes the peak of the impulsive phase where the derivative is maximum. The blue vertical dotted line corresponds to the peak of the 1–15 keV light curve.

within the energy range considered for fitting are identified. Abundances of those elements are left as free parameters in the fitting process along with temperature and emission measure. For example, if the detected spectrum extends beyond the Fe line complex at ~ 6.5 keV, the abundance of Fe is considered as a free parameter. As the Mg and Si lines are well detected in spectra for all one minute intervals, their abundances are left as free parameters in the fitting of all spectra. Abundances of S, Ar, Ca, and Fe are allowed to vary for some of the intervals depending on the detection of the corresponding line complex in the spectrum. We also note that while the XSM observations include the emission from quiescent active region as well, it is observed that even for B-class events the effect of this on the inferred parameters of the flare emission is negligible (Mondal et al. 2021). Hence we do not include pre-flare quiescent emission component separately in this work.

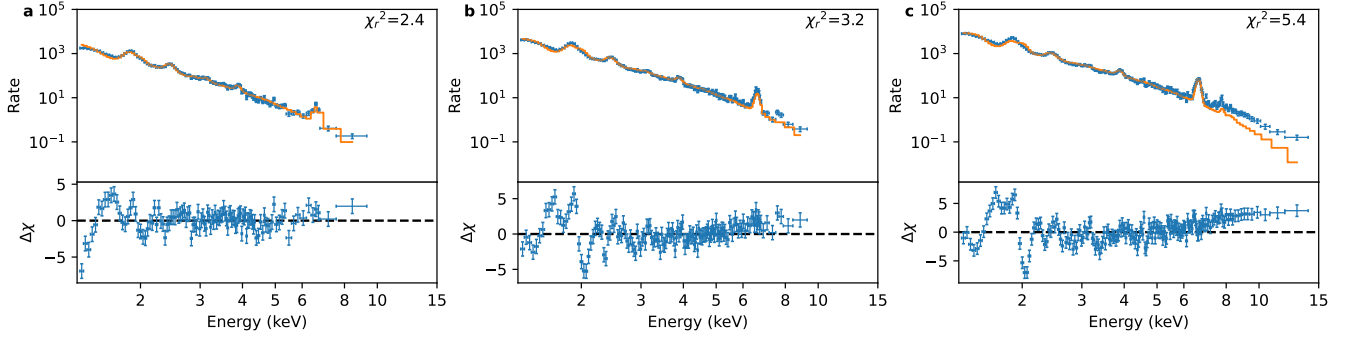


Figure 2. XSM spectra of the three flares (panel **a**: C1.57, panel **b**: C5.70, panel **c**: C8.40) at their impulsive phase peak (marked by vertical dashed lines in Figure 1) fitted with an isothermal model. Orange lines show the best fit models and the lower panels show the residuals.

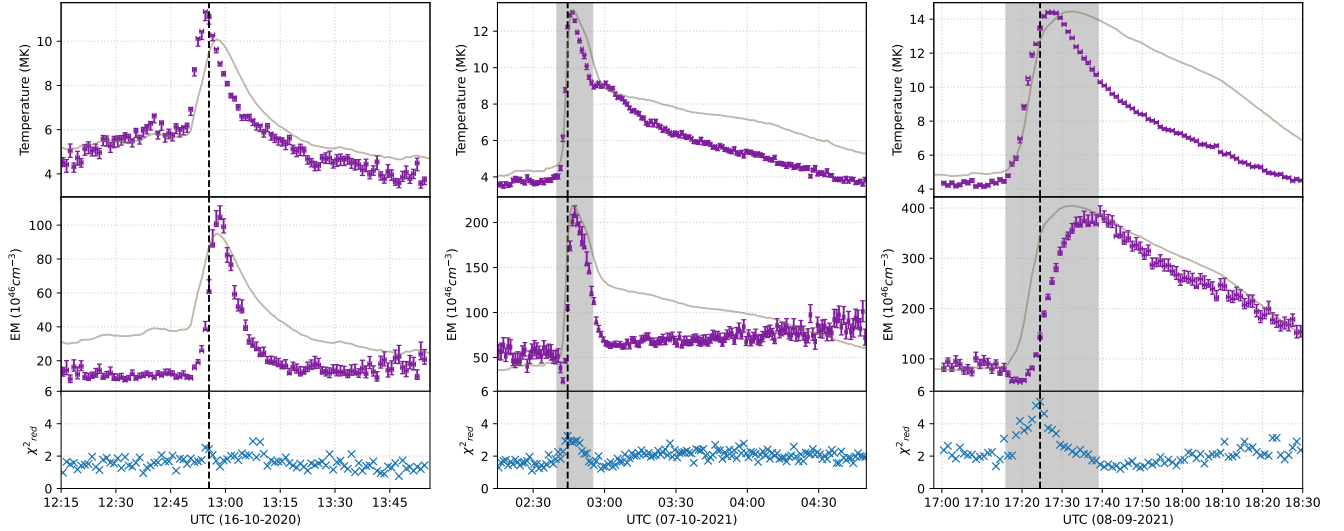


Figure 3. Results of an isothermal fit to the time-resolved spectra of the three flares. Best fit temperature and emission measure with one sigma uncertainties are shown in the top and middle panels. Lower panels show the reduced chi-squared of the spectral fits. Impulsive phase peak times are marked by the vertical dashed lines. For the two brighter events, the reduced chi-squared is seen to be higher around the impulsive peak, marked by the grey shaded region.

Figure 2 shows the observed spectra for a one minute interval at the peak of impulsive phase of the three flares. Best fit isothermal models are overplotted and the residuals are shown in the lower panels. For the weakest event in the sample (2020-10-16), the isothermal model fits the spectra reasonably well, although there are still some systematic residuals present. However, for the other two events, the residual of the spectra with respect to the model and the goodness of fit given in terms of the reduced chi-squared suggest that a single temperature isothermal model does not describe the observations very well.

A similar analysis is carried out for each one minute interval during the flares and the best fit isothermal temperature and emission measure along with the reduced chi-square for the entire duration of the flares are shown in Figure 3. It can be seen from the figure that the isothermal approximation is valid during the pre-flare and decay phases for all three events where the reduced chi-square are within acceptable ranges. For the flare on 16-October-2020, the fit is reasonable for the entire duration of the event. However, during the impulsive phase of the other two events, marked by the grey shaded region in the figure, the reduced chi-square values suggest that the isothermal approximation is no longer valid. The vertical dashed lines in the figure correspond to the peak of the impulsive phase as identified in Figure 1 and it can be seen that the departure from the isothermal model is maximum around these times.

We also note that during the period where the observed spectra deviate from an isothermal model, the fitted temperature and emission measure show rapid variations. From the analysis presented in Appendix A, we conclude that the fast evolution of temperature and emission measure cannot explain the deviations from isothermal models and thus the XSM spectra during the impulsive phase show the presence of multi-thermal plasma.

In order to obtain an idea of the range of temperatures involved, we separately fitted the low energy part of the spectrum that is more sensitive to lower temperature and the high energy part of the spectrum that is more sensitive to higher temperatures. Spectrum below 4 keV and spectrum above 4 keV were fitted with isothermal models as shown in Figure 4. It can be seen that a model with $\log T$ 7.03 provides a reasonable fit to the low energy part of the spectrum while severely under predicting the emission at higher energies. Conversely, a model corresponding to $\log T$ of 7.26 is sufficient to explain the high energy part of the spectrum including the Fe line complex, but significantly deviates from the low energy spectrum and also predicts very different line shapes for the Mg/Si/S line complexes compared to the observations. It should also be noted that the abundances of elements were frozen to the best fit values obtained from an isothermal analysis. However, we find that any reasonable variations in the abundances within the ranges from photospheric to coronal values cannot account for the differences in line strengths between the observation and the model. From this we conclude that at the impulsive peak, temperature distributions extending at least over this range of two temperatures is required to consistently explain the observed spectrum and we explore this in detail in the next section.

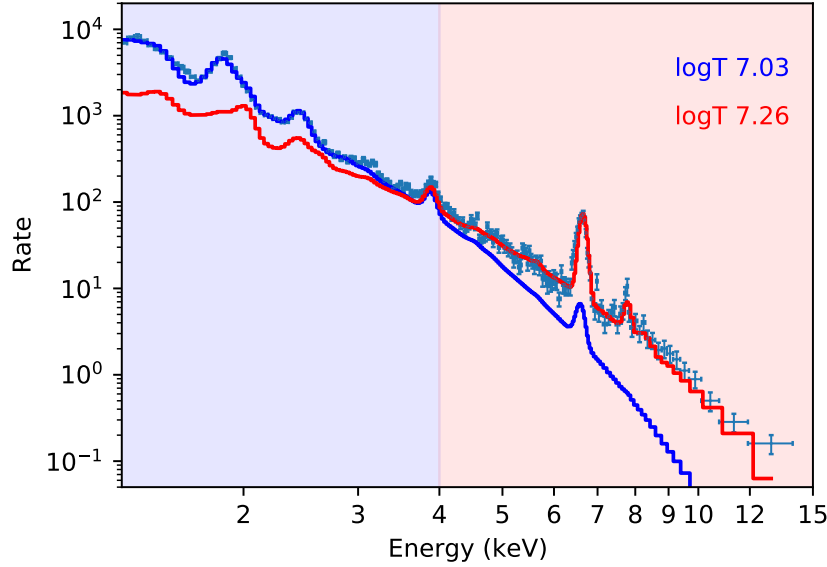


Figure 4. Spectrum during the impulsive phase of the 08-Sep-2021 flare (17:24-17:25 UTC) fitted with two different isothermal models considering only part of the spectrum. The spectrum below 4 keV (blue shaded interval) is fitted to obtain the best fit model shown in blue and a fit to the spectrum above 4 keV (red shaded interval) gives the best fit model shown in red.

4. MULTI-THERMAL PLASMA: DIFFERENTIAL EMISSION MEASURE ANALYSIS

The analysis in the previous section suggests that multi-thermal plasma is present during the impulsive phase of flares. The distribution of plasma at different temperatures can be described by the Differential Emission Measure (DEM), which provides the amount of plasma along the line of sight having temperature between T and $T+dT$ (Del Zanna & Mason 2018). With non-imaging full disk observations, one cannot obtain the spatial distribution of the plasma and in such cases we measure the differential on the volume emission measure (cm^{-3}) over temperature (T) defined as

$$DEM(T) = \frac{d(N_e^2 V)}{dT} (\text{cm}^{-3} \text{K}^{-1}) \quad (1)$$

where V is the volume and N_e is the electron density. Conversely, the volume emission measure is the integral of DEM over temperature as:

$$EM = \int DEM(T) dT \quad (2)$$

Several methods have been developed to infer the DEM from observations in different wavelengths. Two commonly used approaches are direct inversion and forward fitting by χ^2 minimization (see [Del Zanna & Mason \(2018\)](#) for a review of methods for DEM estimation). We follow the χ^2 minimization approach for estimating DEM from the XSM spectra. Often, counts over broad energy bins obtained from the spectra are used as input in DEM analysis. However, based on the analysis of temperature responses of the XSM presented in [Appendix B](#), we find that using the full spectrum as input to DEM analysis provides better diagnostic potential. Thus, the observed spectrum as used in the isothermal analysis previously is used for DEM fitting.

4.1. Emission measure loci

A simple method to assess the distribution of plasma at different temperatures without DEM fitting is to follow the emission measure loci approach ([Del Zanna & Mason 2018](#)). In this approach, the ratio of the observed counts in different spectral channels to the expected counts in the respective channels at different temperatures obtained from theoretical calculations are plotted. The loci of these curves provides an upper limit to the emission measure distribution. If the entire spectrum is consistent with isothermal emission, the curves of different channels intersect at the same point.

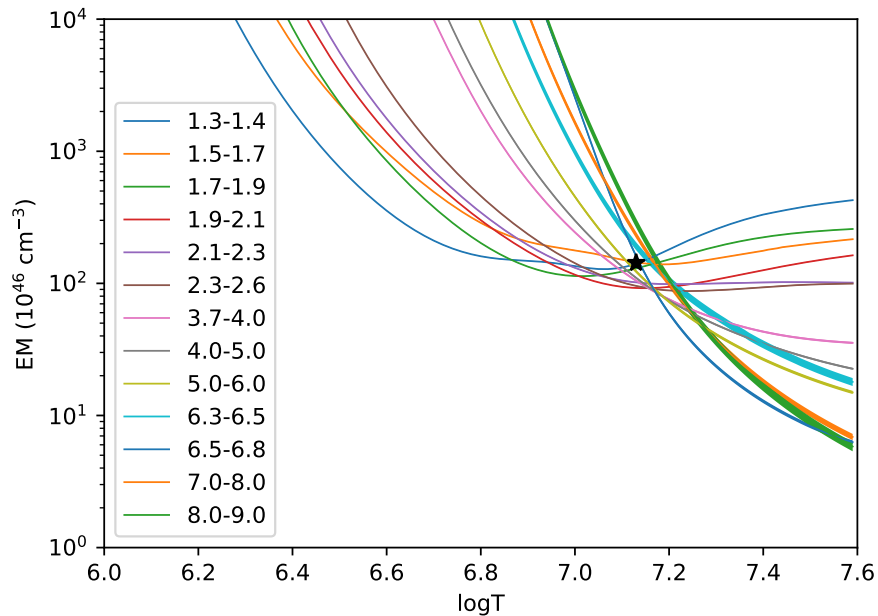


Figure 5. EM loci curves obtained from XSM spectrum during the impulsive peak of the 08-Sep-2021 flare. Each line corresponds to the ratio of the observed counts in the given energy range to the counts predicted by model for an isothermal plasma with the EM of 1 cm^{-3} at different temperatures. The width of the lines takes into account the one sigma uncertainties of the observed counts. The best fit isothermal temperature and emission measure is shown by the black star.

We plot the EM loci curves for the XSM spectrum at the impulsive peak of the 08-Sep-2022 flare in [Figure 5](#). While in principle there can be a curve for each spectral channel of XSM, in order to avoid over-crowding of the figure, we show loci curves for spectral channels near the different line complexes and of some continuum channels grouped together. The expected counts in each channel range are obtained from the model spectra convolved with the instrument spectral response as was done in obtaining the temperature response discussed in [Appendix B](#). It can be seen from the figure that the curves do not intersect at a single point. While the isothermal fit result shown by the black star in the figure is at the intersection of a few loci curves, many others do not pass through that point as one would expect based on the residuals seen in the isothermal fits.

4.2. Multi-thermal model fitting

EM loci curves above provide an upper limit to the true DEM distribution. While the DEM distribution can have any shape below this upper limit, in order to obtain some estimates of the DEM, we start with few simple functional forms. We note that for the DEM estimation, it is necessary to use all spectral channels of the detector, as discussed in the Appendix B. Thus, we follow a forward folding approach to estimate the DEM distribution from the XSM spectra. Model spectrum from an assumed DEM distribution defined by few parameters is computed and then fitted to the observation after folding through the instrument response using PyXSPEC to obtain the best fit DEM parameters. We consider three multi-thermal models in the present analysis viz. two-temperature, Gaussian DEM, and double Gaussian DEM.

The simplest extension of an isothermal model is a two temperature model which is the sum of two isothermal models with independent temperatures and emission measures. This DEM with two delta functions is considered as the analysis in the previous section suggested that two different temperatures could explain the lower and higher energy part of the spectrum. Similar two-temperature models have been used in previous studies to model flare spectra (for e.g., Caspi & Lin 2010). The observed spectra are fitted with a model defined as the addition of two isothermal models (described in the previous section) with two temperatures, respective emission measures, and abundances of different elements as free parameters.

For a broader temperature distribution, a natural choice is a Gaussian distribution (Aschwanden et al. 2015) defined by the temperature at the peak EM (T_p), the peak emission measure (EM_p), and the width of the Gaussian (σ) as:

$$DEM(T) = EM_p \exp\left(-\frac{(\log(T) - \log(T_p))^2}{2\sigma^2}\right) \quad (3)$$

We have implemented a model providing the X-ray spectra for Gaussian DEM within XSPEC, named `chgausdem`⁴, for the analysis of the data. This is obtained by the weighted addition of spectra over the grid of temperatures with the emission measure at each temperature as defined by the Gaussian function. Much like the isothermal model, the Gaussian DEM model also has provision to vary abundances of individual elements.

While a single Gaussian allows a broad DEM, it is constrained to have only a single maximum. To accommodate multiple peaks in the DEM, it can be approximated with multiple Gaussians (Caspi et al. 2014). However, the number of free parameters will be prohibitively large in that case. Instead we consider a DEM function composed of two Gaussians with their peak temperatures, emission measures, and widths as independent parameters. This model is a more realistic version of the two-temperature isothermal model allowing finite width to the EM distributions at two temperatures.

4.2.1. DEM fit results

We carried out the spectral analysis of the flares with these three multi-thermal models with the DEM parameters and abundances of elements with prominent lines as free parameters. As an example, the results of the fit to the spectrum during the impulsive phase of the 08-Sep-2021 flare are shown in Figure 6. The top panel of Figure 6a shows the spectrum overplotted with the best fit models for each case including the isothermal fit presented in the previous section for comparison, whereas the bottom four panels show residuals of the fit with different models. Figure 6b shows the best fit differential emission measure distributions obtained in each case. For the two-temperature model and isothermal models, vertical lines show the temperature and emission measure.

From the figure, it can be seen that the multi-thermal models provide a much better fit to the observed spectrum as compared to the isothermal model. Residuals near the Si line complex and at higher energies are substantially less in the case of all multi-thermal models. The reduced chi-squared for the multi-thermal models are within the acceptable range as compared to the much higher values for the isothermal model. An important point to note is the fact that different multi-thermal models predict nearly identical X-ray spectra and hence statistically all multi-thermal models provide equally acceptable fits to the observations.

The best fit two-temperature model includes one component at temperatures below 10 MK having higher emission measure and another component at higher temperature with a slightly lower emission measure. The isothermal temperature and emission measure lies in between the two temperature components obtained from this fit. The best

⁴ <https://github.com/xastprl/chspec>

fit Gaussian DEM has a very broad distribution peaking at $\log T$ of about 6.8 and having significant emission measure at lower and higher temperatures. The double Gaussian DEM model fit resulted in two relatively narrower Gaussians having peak temperatures closer to the temperatures obtained from the two-T fit to the spectra.

In order to estimate the uncertainty on the best fit DEM models, we carried out a Markov Chain Monte Carlo (MCMC) analysis. MCMC chains were run within PyXSPEC with the DEM parameters and abundances as free parameters as in the spectral fitting and selected parameters from the chain are written out. DEMs computed from a few randomly selected set of parameters from the MCMC chain results are shown as thin lines in Figure 6b. The spread of these DEMs show typical uncertainties in the fitted DEM. For the two-temperature models, the lower temperature component is less constrained compared to the higher temperature component. In the case of the Gaussian model, we note that the DEM at lower temperatures are less constrained. This is not a surprising result as XSM spectra have relatively lower sensitivity to plasma at those temperatures.

We then fitted the spectrum during each one minute interval with the three models to obtain the temporal evolution of the flare plasma parameters. As was seen in the previous section, the faintest flare event in the sample is consistent with an isothermal model through out the duration of the flare. We therefore exclude that event from the multi-thermal analysis. The other two events were fitted with each of the three multi-thermal models and the results obtained are shown in Figure 7. Panel a corresponds to the 08-Sep-2021 flare, while panel b corresponds to the 07-Oct-2021 flare. For each flare, the three vertical panels show the time evolution of the DEM obtained from the two-temperature model, the Gaussian model, and the double Gaussian model as marked in the figure. Colors correspond to the value of emission measure at each temperature at respective time intervals. The isothermal temperature obtained are overplotted in each case. The lower most panels show the reduced chi-square of the fit with each of the multi-thermal models along with that from the isothermal fits for comparison.

From the figure, it can be seen that during the pre-flare period and the decay phase of both the flares (marked by grey shade in the figure) all three models converge to a narrow range of temperatures close to the isothermal temperature. With the two-temperature and double Gaussian models, the temperatures of the two components attain the same value (isothermal temperature) during the early and decay phase of the flares. This is not very surprising as the spectra during these intervals were consistent with an isothermal model. During these periods, there is no notable difference in the reduced chi-square of the fit with different multi-thermal models and the isothermal model.

During the impulsive phase where the isothermal model is clearly not valid, we can see a consistently better fit to the spectrum with the multi-thermal model at all time bins similar to the example shown in Figure 6. Also, the three models have identical quality of fit with the observed spectrum. From the evolution of DEM shown in Figure 7, we can see that the two-temperature fits result in two distinct temperature components during this interval for both the flares. A single Gaussian model results in a very broad emission measure distributions during the impulsive phase while the double Gaussian model generally shows two narrow Gaussians peaked at distinct temperatures very similar to the two-temperature fit.

The single Gaussian models predict significant EM at lower temperature where soft X-ray spectra observed by the XSM has low sensitivity. It is also seen from the MCMC analysis that the uncertainties on the DEM at low temperatures are higher. While the two-temperature DEM is obviously an over simplification, we believe that the two Gaussian DEM is most likely the model closer to the true DEM distribution during the impulsive phase of the flares.

4.2.2. Elemental abundances of low FIP elements

Another interesting result from our time resolved spectral analysis concerns the variation of the elemental abundances. In addition to the plasma emission measure distribution parameters, the abundances of elements were also free parameters during the fit and we obtain the abundances of various elements during the evolution of the flares. Figure 8 shows the best fit abundances of the low FIP elements Mg, Si, and Fe during the course of the 08-Sep-2021 flare. Different colors correspond to the abundances obtained from fitting with different multi-thermal models considered in the present analysis. In the figure, the pink dashed line corresponds to the coronal abundances given by Feldman (1992), the grey dashed line corresponds to the active region coronal abundances from Del Zanna (2013), and the yellow dashed line corresponds to the photospheric abundances from Asplund et al. (2009).

We see that the abundances estimated from three different DEM models match very closely except for slight differences seen in the abundances obtained from Gaussian DEM fit during the impulsive phase. In any case, the overall trend seen in the variation of abundances during the flare is similar with all three models. The abundances of Mg and Si was close to the typical coronal abundances before the the flare and they reduce to values close to photospheric

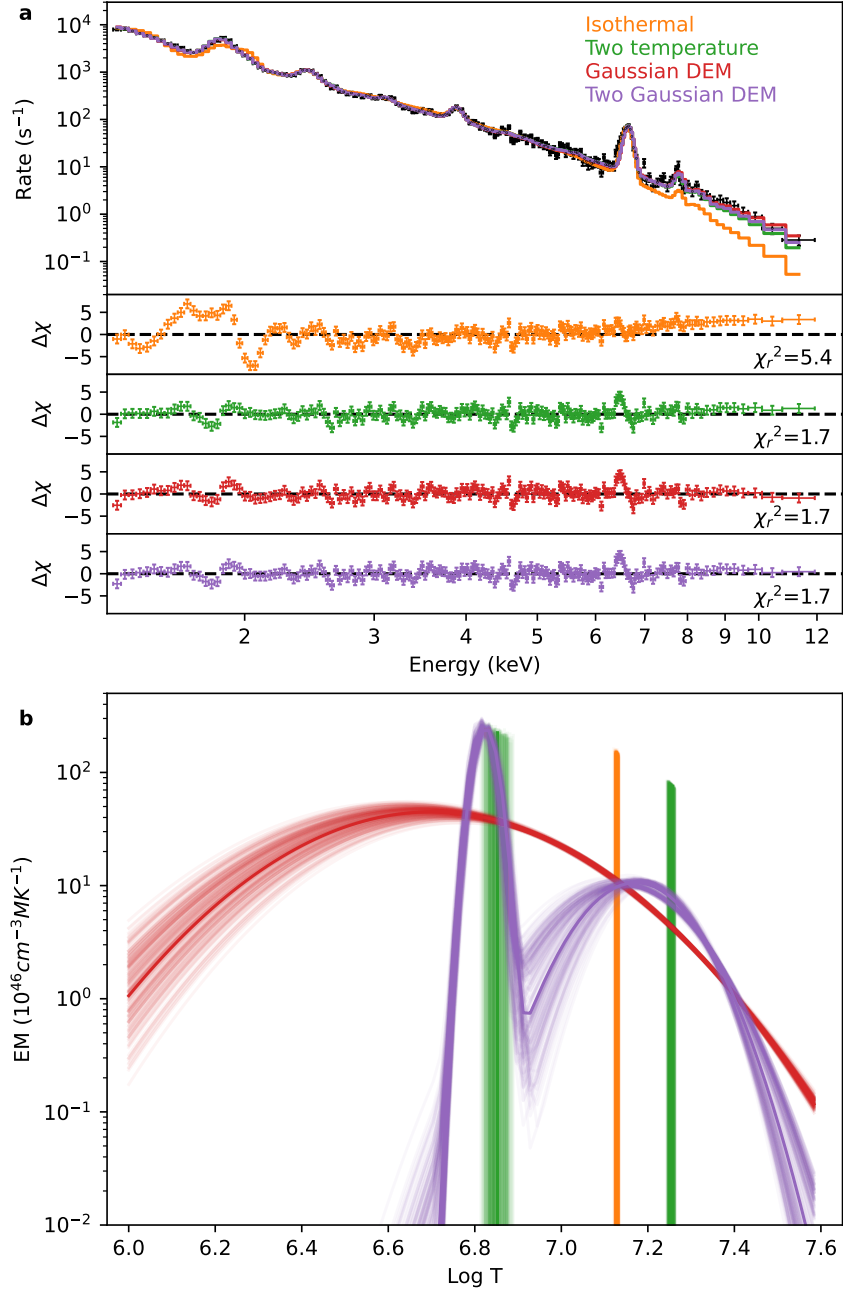


Figure 6. (a) XSM spectrum of the impulsive peak of the 08-Sep-2021 flare fitted with different multi-thermal models and isothermal model. The best fit with each model are shown in different colors and the residuals are shown in the lower panels. (b) The best fit DEM models from the spectral fit in the panel a are shown with the respective colors. Lighter color lines correspond to DEMs from 100 random samples from the MCMC analysis showing the uncertainty of the derived DEM models.

abundances during the rise phase of the flare. The abundances are seen to return to the coronal values during the decay phase of the flare. As the Fe abundance measurement is available only during the periods near the flare peak, the entire evolution is not observed in the case of Fe. A similar trend of abundance variations was reported by [Mondal et al. \(2021\)](#) for smaller B-class events observed by the XSM. The present results show that the same effect is seen during larger flares and that it is seen for Fe abundances too which was not measurable during the smaller events.

5. DISCUSSION AND SUMMARY

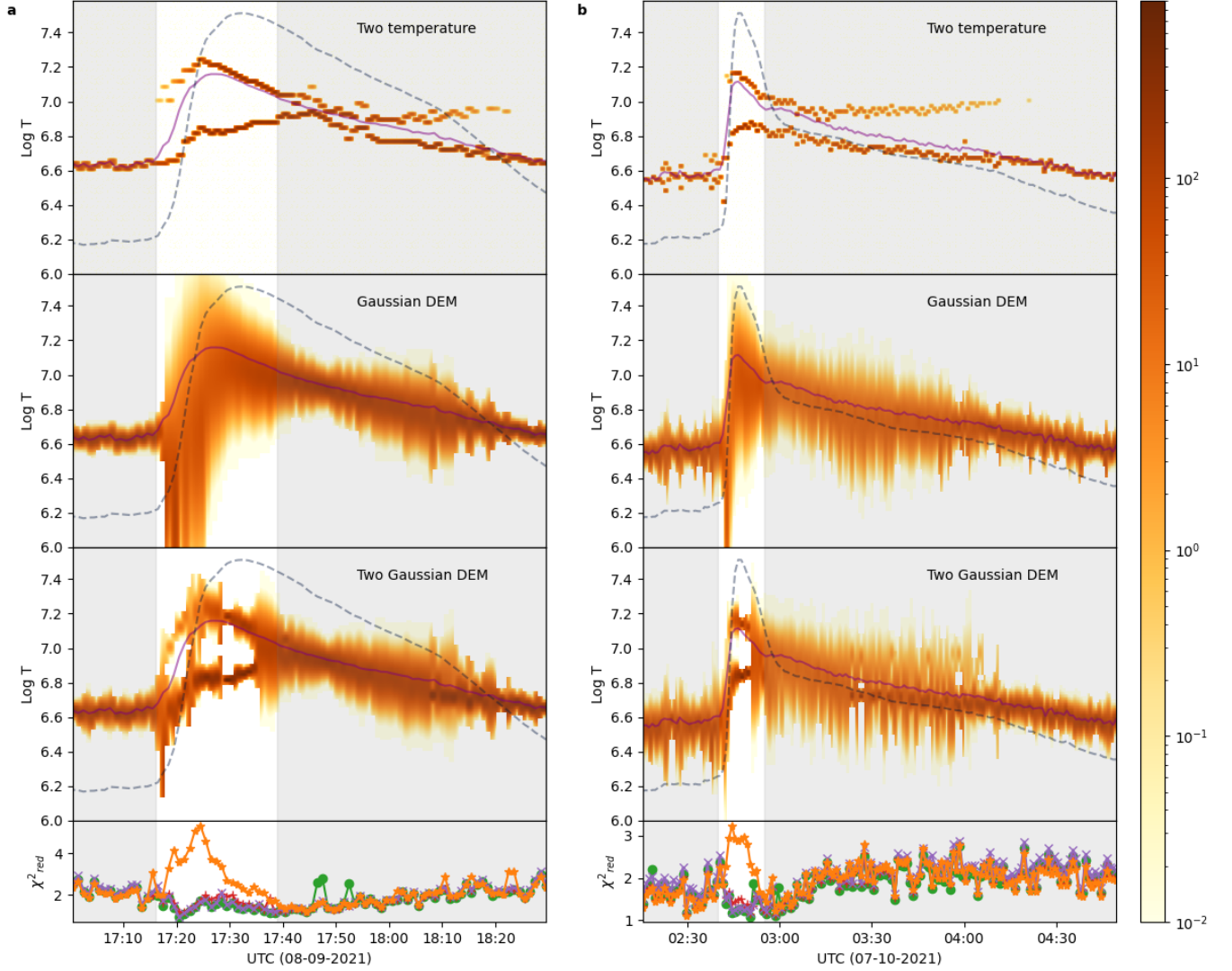


Figure 7. Differential Emission Measure (DEM) evolution during the 08-Sep-2021 flare (a) and the 07-Oct-2021 flare (b) obtained from spectral fitting. The top three panels show DEM with two-temperature, Gaussian, and double Gaussian models, respectively. Color represents the EM in units of $10^{46} \text{cm}^{-3} \text{MK}^{-1}$. The isothermal temperature measurements (purple solid line) and 1–15 keV X-ray light curves (dashed line) are also shown for reference. The reduced chi-squared of the fit with two-temperature (green), Gaussian (red), and double Gaussian (purple) are shown in the lower most panels. The reduced chi-squared for the isothermal fit are shown in orange for comparison. Intervals when the isothermal and multi-thermal models have a similar fit to the spectra are greyed out and during the remaining period in the impulsive phase, the DEM models provide a much better fit to the spectra in comparison with the isothermal model.

We have presented time-resolved analyses of the soft X-ray spectra of three GOES C-class flares using observations with the Chandrayaan-2 XSM. While the spectra during the early and decay phases of the flares are consistent with an isothermal model, the same is not true for the impulsive phase of the higher intensity events (i.e. C5.7 and C8.4 flares). Spectra were then fitted with three different multi-thermal models where DEMs are described with simple parameterized functions. We find that all three DEM models provide equally good fits to the observations, better than the isothermal model. We find that the spectra during the impulsive phase are consistent with the plasma having either a very broad temperature distribution or a double peaked distribution. The lower temperature part of the broad single Gaussian DEMs are not well constrained with XSM observations alone and is possibly adjusted such that the

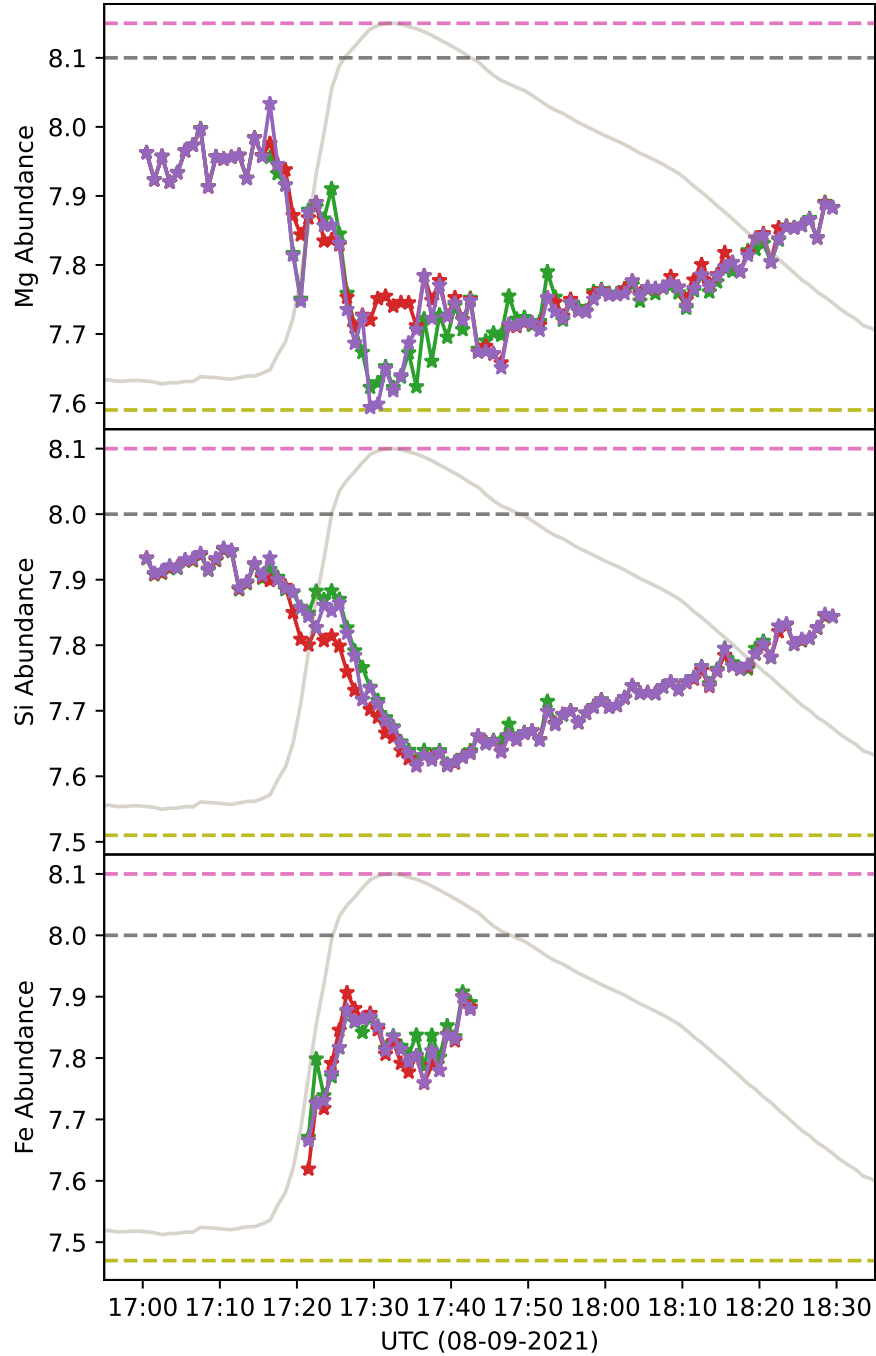


Figure 8. Measured abundances of Mg, Si, and Fe during the 08-Sep-2021 flare obtained from spectral fitting considering three different multi-thermal models: two-temperature (green), Gaussian (red), and double Gaussian (purple), are shown. Coronal abundances from [Feldman \(1992\)](#) and [Del Zanna \(2013\)](#) as well as photospheric abundances from [Asplund et al. \(2009\)](#) are shown with purple, grey, and yellow dashed lines, respectively. The X-ray light curve is shown in grey for reference.

higher temperature part fits the spectra well. This is not the case with the double peaked DEM distributions and thus this is more likely to be closer to the actual plasma parameters.

The observed characteristics of the DEM evolution during the flares, such as broader DEM at the impulsive phase and narrow DEM during the decay phase, are similar to those reported earlier ([Warren et al. 2013](#); [Caspi et al. 2014](#)).

Double peaked structures of DEM for solar flares observed in this study have also been observed using the RESIK X-ray spectrograph (Sylwester et al. 2006; Kepa et al. 2008). If the DEM is indeed double peaked during the impulsive phase, as we infer from the XSM spectra, it is likely that the two distinct temperature components correspond to the emission from the directly heated plasma in the loop/loop-top and the evaporated chromospheric material filling the flaring loops. Hard X-ray imaging observations have shown the presence of coronal loop top sources in addition to the chromospheric foot point sources for several flares (Krucker et al. 2008). Caspi & Lin (2010) have shown that the RHESSI observations of an X-class flare consists of two distinct temperature components: one super-hot (> 30 MK) component located higher in the corona and a hot component arising from the foot points. Although the higher temperatures in our present observations are not as high as the super-hot component reported in Caspi & Lin (2010), it is not unexpected since the flares we have studied here (C-class) are substantially weaker. The fact that the higher temperature component rises faster during the early phase of the flare as compared to the lower temperature component further supports the supposition that the the former may be associated with the direct heating near the reconnection region.

The evolution of abundances of low-FIP elements from coronal to near photospheric and back to coronal values are similar to the observations by Mondal et al. (2021) for B-class flares. The reduction of abundances to near photospheric values during the rising phase of the flares is consistent with the chromospheric evaporation. The quick recovery back to coronal abundances favors the involvement of flare induced Alfvén waves causing fractionation (Mondal et al. 2021). Unlike Mg and Si abundances that reach very close to photospheric values during the flare peak, the Fe abundances are found to be in between photospheric and coronal values at flare peak. One possibility is that the abundances of the two distinct temperature components are different and that fitting the same abundance parameter for both components may have resulted in an intermediate value. If the hotter component is indeed arising from coronal loops, it would have coronal abundances while the material evaporating from the chromospheric foot points would have photospheric abundances. As the hotter component would produce more Fe line emission compared to that of Mg or Si (see Figure 4), the abundances measured considering the same values for both components will effect Fe more and this is reflected in the observations. However, this could not be confirmed with the present data as fitting with different Fe abundance parameters for the two components did not yield a consistent results. It is supported by the fact that previous studies of Fe abundances during flare peaks using the observations of higher temperature lines with RHESSI by Phillips & Dennis (2012) found abundances closer to coronal values as opposed to reports of close to photospheric abundances from lower temperature lines (for e.g. Del Zanna & Woods 2013). It is also possible that there are some other factors such as non-thermal broadening of Fe lines that are not included in the model which could be responsible for the difference in Fe abundance values. Spectral fits shown in Figure 6a with all multi thermal models show small but visible residuals near the Fe line complex. We plan to further investigate this in detail in the future.

While the XSM spectra can provide some insights into the broader temperature distributions, in order to constrain the DEM over a wide range of temperatures and to see where the different temperatures might be originating, it would be useful to combine observations from multiple instruments sensitive to different temperature ranges which also have spatial information. For example, observations with some channels of SDO AIA are sensitive to lower temperatures as compared to the XSM and thus these instruments complement each other. We plan to take up joint fitting of AIA and XSM observations to have better constraints to the lower temperature part of the DEM. Del Zanna et al. (2022) has made comparisons of the model spectrum obtained using AIA DEM with the XSM observed spectrum of a B class event to find that they match very well showing that it would be possible to carry out such joint fitting. On other other hand, the DEM associated with higher temperature plasma as well as the non-thermal particles can be better constrained with observations in hard X-rays. Thus, observations in both soft and hard X-rays of flares will allow us to constrain the characteristics of both the thermal and non-thermal particle populations simultaneously, which has implications on improving our understanding on the energy partition in flares. In this context, such complementary observations for XSM are available with the Spectrometer Telescope for Imaging X-rays (STIX, Krucker et al. 2020) on board the Solar Orbiter mission and we plan to use these in the future.

The results from the present work points towards a complex heating process of coronal loops during flares. The observation of two distinct temperature components seems to support the role of direct heating of coronal loop-tops by magnetic reconnection and secondary heating of post-reconnected loops by chromospheric evaporation. This is also consistent with the evolution of the elemental abundances. The XSM has been operating for about three years now and is expected to be operational for few more years possibly into the next solar maximum. Soft X-ray spectra

obtained with the XSM combined with observations in other wavelengths provide a unique opportunity for studying the thermal evolution of flares to further our understanding of plasma heating processes in solar flares.

ACKNOWLEDGMENTS

We acknowledge the use of data from the Solar X-ray Monitor (XSM) on board the Chandrayaan-2 mission of the Indian Space Research Organisation (ISRO), archived at the Indian Space Science Data Centre (ISSDC). The XSM was developed by Physical Research Laboratory (PRL) with support from various ISRO centers. We thank various facilities and the technical teams from all contributing institutes and Chandrayaan-2 project, mission operations, and ground segment teams for their support. Research work at PRL is supported by the Department of Space, Govt. of India. We acknowledge the support from Royal Society through the international exchanges grant No. IES\R2\170199. GDZ HEM and YR acknowledge support from STFC (UK) via the consolidated grant to the atomic astrophysics group at DAMTP, University of Cambridge (ST/T000481/1).

Facilities: Chandrayaan-2(XSM)

Software: XSM DAS (Mithun et al. 2021b), XSPEC (Arnaud 1996) and PyXSPEC, Python, matplotlib

APPENDIX

A. EFFECT OF TEMPORAL AVERAGING

In order to investigate whether the fast evolution of temperature and emission measure during the integration period of one minute is the reason why the observed spectrum is not consistent with a single temperature, we carried out the following analysis. As the temperature and emission measure show smooth variations, we interpolate the fitted parameters from one minute spectra to obtain the temperature and emission measure for the event on 08-Sep-2022 at every second as shown in Figure 9a. Then, model spectra for each one minute interval is obtained by summing the isothermal spectral at each second with the respective temperature and emission measure. It may be noted that the abundances for each one second were set to the best fit value obtained for the one minute interval. This model is then compared with the observed spectrum as shown in Figure 9b. We find that this model, which takes into account the evolution of plasma parameters within the integration time, is also not consistent with the observed spectrum and has only marginally better goodness of fit compared to the isothermal fit. We obtain the same result for other time intervals. We also carried out spectral fitting for shorter integration times and although the statistical uncertainties are higher, inconsistency of soft X-ray spectra with isothermal models in the impulsive phase remains apparent. We therefore conclude that the X-ray spectra with the XSM during the impulsive phase shows the presence of multi-thermal plasma.

B. LINE PROFILES WITH XSM AND TEMPERATURE RESPONSE

In order to understand the sensitivity of XSM spectra to different temperatures, we generated temperature responses of various XSM energy bands. Model spectra for a range of temperatures are generated from the CHIANTI model and then convolved with the XSM response matrix to obtain the counts in different energy bands arising from plasma at different temperatures. Figure 10a shows the temperature response of the XSM energy bands of 1 keV in the entire energy range from 1 - 15 keV. It can be noted that all except two energy bands have a rather similar shape of the temperature response, as those energy bands are primarily dominated by continuum emission. The 1-2 keV and 6-7 keV bands include strong line emission from Mg and Si and Fe, respectively and hence show a slightly different behaviour. The 1-2 keV band has a local maximum in the temperature response near $\log T$ of 7.1. Figure 10b shows the normalized temperature response of some of the energy channels of the XSM in the Si line complex, which explains the local maximum seen in the overall energy range response. It can be seen that different energy channels in the Si line complex are most sensitive to different temperatures in the range of $\log T$ from ~ 6.9 to ~ 7.3 . This is due to the different formation temperatures of various lines from different ionization states of Si that are blended together in the observed line complex and even though the lines are not completely resolved, the spectral resolution of the XSM allows

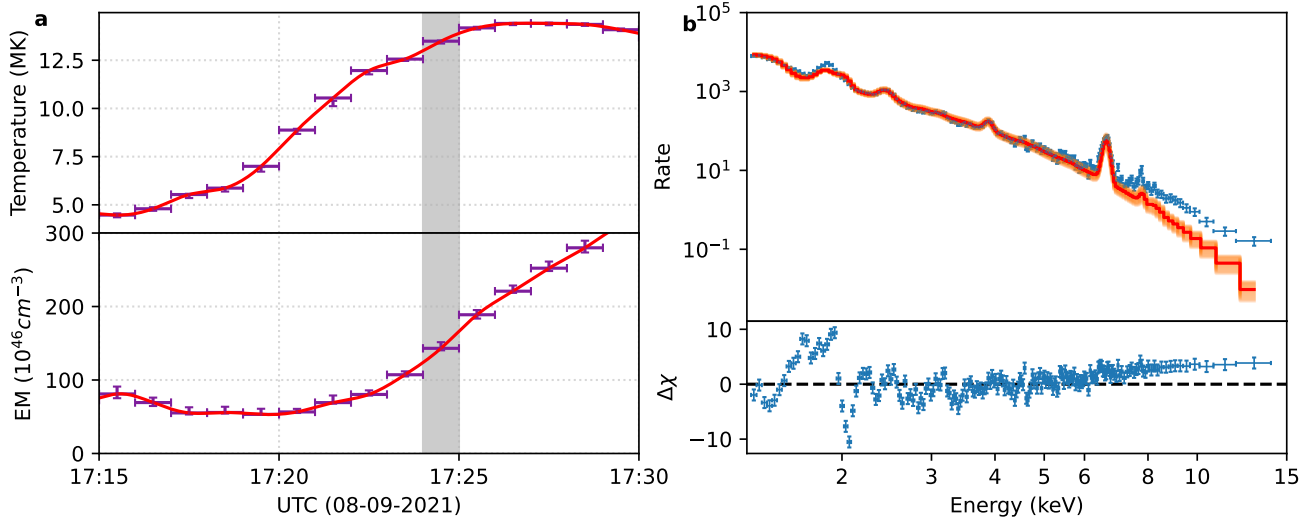


Figure 9. Panel **a** shows temperature and emission measure of the 08-Sep-2021 flare. Red line is interpolated values from the measurements at one minute. Spectrum for the grey shaded interval (17:24-17:25) is shown in panel **b** with blue data points. Isothermal models corresponding to the interpolated temperature and EM for each one second within the interval are shown with light orange lines and the average model considering the variation of temperature and EM is shown by solid orange line. Residuals of the observed spectrum with this average model (solid orange line in upper panel) are shown in the lower panel.

the disentanglement of the emission from different temperature ranges. We can understand this better from panel c of Figure 10 which shows the normalized spectra near the Si line complex for different range of temperatures. Similarly, the change in observed line profile for the Fe line complex is shown in panel d of Figure 10, although the differences are less in this case.

We infer that the XSM spectra, especially the Si line complex, shows a distinct response at different temperatures allowing the disentanglement of different temperature components in the range of $\log T$ 6.9-7.3. As the line shape is the most prominent feature to distinguish different temperatures, any multi-thermal analysis with XSM spectra use the full spectrum rather than using counts in broader energy bins.

REFERENCES

- Arnaud, K. A. 1996, in *Astronomical Society of the Pacific Conference Series*, Vol. 101, *Astronomical Data Analysis Software and Systems V*, ed. G. H. Jacoby & J. Barnes, 17
- Aschwanden, M. J., Boerner, P., Caspi, A., et al. 2015, *SoPh*, 290, 2733, doi: [10.1007/s11207-015-0790-0](https://doi.org/10.1007/s11207-015-0790-0)
- Asplund, M., Grevesse, N., Sauval, A. J., & Scott, P. 2009, *ARA&A*, 47, 481, doi: [10.1146/annurev.astro.46.060407.145222](https://doi.org/10.1146/annurev.astro.46.060407.145222)
- Athiray, P. S., Vievering, J., Glesener, L., et al. 2020, *ApJ*, 891, 78, doi: [10.3847/1538-4357/ab7200](https://doi.org/10.3847/1538-4357/ab7200)
- Awasthi, A. K., Sylwester, B., Sylwester, J., & Jain, R. 2016, *ApJ*, 823, 126, doi: [10.3847/0004-637X/823/2/126](https://doi.org/10.3847/0004-637X/823/2/126)
- Benz, A. O. 2017, *Living Reviews in Solar Physics*, 14, 2, doi: [10.1007/s41116-016-0004-3](https://doi.org/10.1007/s41116-016-0004-3)
- Carmichael, H. 1964, in *NASA Special Publication*, Vol. 50, 451
- Caspi, A., & Lin, R. P. 2010, *ApJL*, 725, L161, doi: [10.1088/2041-8205/725/2/L161](https://doi.org/10.1088/2041-8205/725/2/L161)
- Caspi, A., McTiernan, J. M., & Warren, H. P. 2014, *ApJL*, 788, L31, doi: [10.1088/2041-8205/788/2/L31](https://doi.org/10.1088/2041-8205/788/2/L31)
- Cheung, M. C. M., Boerner, P., Schrijver, C. J., et al. 2015, *ApJ*, 807, 143, doi: [10.1088/0004-637X/807/2/143](https://doi.org/10.1088/0004-637X/807/2/143)
- Del Zanna, G. 2013, *A&A*, 558, A73, doi: [10.1051/0004-6361/201321653](https://doi.org/10.1051/0004-6361/201321653)
- Del Zanna, G., Andretta, V., Cargill, P. J., et al. 2021a, *Frontiers in Astronomy and Space Sciences*, 8, 33, doi: [10.3389/fspas.2021.638489](https://doi.org/10.3389/fspas.2021.638489)
- Del Zanna, G., Dere, K. P., Young, P. R., & Landi, E. 2021b, *ApJ*, 909, 38, doi: [10.3847/1538-4357/abd8ce](https://doi.org/10.3847/1538-4357/abd8ce)
- Del Zanna, G., & Mason, H. E. 2018, *Living Reviews in Solar Physics*, 15, 5, doi: [10.1007/s41116-018-0015-3](https://doi.org/10.1007/s41116-018-0015-3)
- Del Zanna, G., & Woods, T. N. 2013, *A&A*, 555, A59, doi: [10.1051/0004-6361/201220988](https://doi.org/10.1051/0004-6361/201220988)

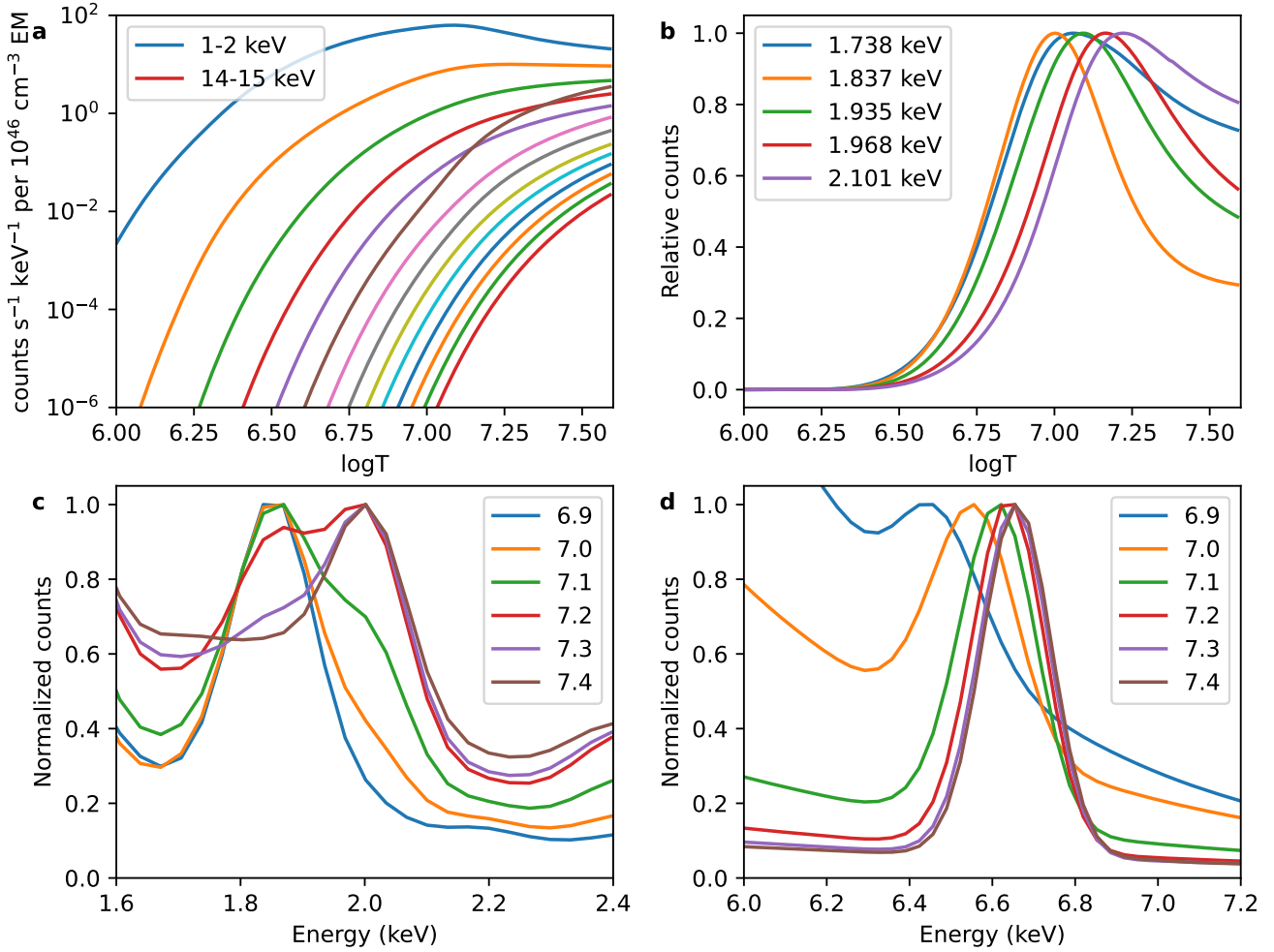


Figure 10. Panel a shows temperature response of the XSM in 1 keV energy bins from 1 to 15 keV in sequence while panel b has normalized temperature responses of selected energy channels near the Si line complex. Simulated XSM spectra near the Si and Fe line complexes at different temperatures are shown in panels c and d, respectively.

Del Zanna, G., Mondal, B., Rao, Y. K., et al. 2022, *ApJ*, 934, 159, doi: [10.3847/1538-4357/ac7a9a](https://doi.org/10.3847/1538-4357/ac7a9a)
 Doschek, G. A. 1990, *ApJS*, 73, 117, doi: [10.1086/191443](https://doi.org/10.1086/191443)
 Feldman, U. 1992, *PhysS*, 46, 202, doi: [10.1088/0031-8949/46/3/002](https://doi.org/10.1088/0031-8949/46/3/002)
 —. 1996, *Physics of Plasmas*, 3, 3203, doi: [10.1063/1.871605](https://doi.org/10.1063/1.871605)
 Gburek, S., Sylwester, J., Kowalinski, M., et al. 2013, *SoPh*, 283, 631, doi: [10.1007/s11207-012-0201-8](https://doi.org/10.1007/s11207-012-0201-8)
 Goryaev, F. F., Parenti, S., Urnov, A. M., et al. 2010, *A&A*, 523, A44, doi: [10.1051/0004-6361/201014280](https://doi.org/10.1051/0004-6361/201014280)
 Hirayama, T. 1974, *SoPh*, 34, 323, doi: [10.1007/BF00153671](https://doi.org/10.1007/BF00153671)
 Jain, R., Dave, H., Shah, A. B., et al. 2005, *SoPh*, 227, 89, doi: [10.1007/s11207-005-1712-3](https://doi.org/10.1007/s11207-005-1712-3)
 Kepa, A., Sylwester, B., Siarkowski, M., & Sylwester, J. 2008, *Advances in Space Research*, 42, 828, doi: [10.1016/j.asr.2007.05.054](https://doi.org/10.1016/j.asr.2007.05.054)

Kepa, A., Sylwester, B., Sylwester, J., Gryciuk, M., & Siarkowski, M. 2018, *Journal of Atmospheric and Solar-Terrestrial Physics*, 179, 545, doi: [10.1016/j.jastp.2018.09.004](https://doi.org/10.1016/j.jastp.2018.09.004)
 Kopp, R. A., & Pneuman, G. W. 1976, *SoPh*, 50, 85, doi: [10.1007/BF00206193](https://doi.org/10.1007/BF00206193)
 Krucker, S., Battaglia, M., Cargill, P. J., et al. 2008, *A&A Rv*, 16, 155, doi: [10.1007/s00159-008-0014-9](https://doi.org/10.1007/s00159-008-0014-9)
 Krucker, S., Hurford, G. J., Grimm, O., et al. 2020, *A&A*, 642, A15, doi: [10.1051/0004-6361/201937362](https://doi.org/10.1051/0004-6361/201937362)
 Laming, J. M., Adams, J., Alexander, D., et al. 2010, *arXiv e-prints*, arXiv:1011.4052, <https://arxiv.org/abs/1011.4052>
 Matthews, S. A., Reid, H. A. S., Baker, D., et al. 2021, *Experimental Astronomy*, doi: [10.1007/s10686-021-09798-6](https://doi.org/10.1007/s10686-021-09798-6)

- McTiernan, J. M., Caspi, A., & Warren, H. P. 2019, *ApJ*, 881, 161, doi: [10.3847/1538-4357/ab2fcc](https://doi.org/10.3847/1538-4357/ab2fcc)
- Mithun, N. P. S., Vadawale, S. V., Sarkar, A., et al. 2020, *SoPh*, 295, 139, doi: [10.1007/s11207-020-01712-1](https://doi.org/10.1007/s11207-020-01712-1)
- Mithun, N. P. S., Vadawale, S. V., Shanmugam, M., et al. 2021a, *Experimental Astronomy*, 51, 33, doi: [10.1007/s10686-020-09686-5](https://doi.org/10.1007/s10686-020-09686-5)
- Mithun, N. P. S., Vadawale, S. V., Patel, A. R., et al. 2021b, *Astronomy and Computing*, 34, 100449, doi: <https://doi.org/10.1016/j.ascom.2021.100449>
- Mondal, B., Sarkar, A., Vadawale, S. V., et al. 2021, *ApJ*, 920, 4, doi: [10.3847/1538-4357/ac14c1](https://doi.org/10.3847/1538-4357/ac14c1)
- Moore, C. S., Caspi, A., Woods, T. N., et al. 2018, *SoPh*, 293, 21, doi: [10.1007/s11207-018-1243-3](https://doi.org/10.1007/s11207-018-1243-3)
- Narendranath, S., Sreekumar, P., Pillai, N. S., et al. 2020, *SoPh*, 295, 175, doi: [10.1007/s11207-020-01738-5](https://doi.org/10.1007/s11207-020-01738-5)
- Neupert, W. M. 1968, *ApJL*, 153, L59, doi: [10.1086/180220](https://doi.org/10.1086/180220)
- Phillips, K. J. H., & Dennis, B. R. 2012, *ApJ*, 748, 52, doi: [10.1088/0004-637X/748/1/52](https://doi.org/10.1088/0004-637X/748/1/52)
- Shanmugam, M., Vadawale, S. V., Patel, A. R., et al. 2020, *Current Science*, 118, 45, doi: [10.18520/cs/v118/i1/45-52](https://doi.org/10.18520/cs/v118/i1/45-52)
- Sturrock, P. A. 1966, *Nature*, 211, 695, doi: [10.1038/211695a0](https://doi.org/10.1038/211695a0)
- Su, Y., Veronig, A. M., Hannah, I. G., et al. 2018, *ApJL*, 856, L17, doi: [10.3847/2041-8213/aab436](https://doi.org/10.3847/2041-8213/aab436)
- Sylwester, B., Sylwester, J., Kepa, A., et al. 2006, *Solar System Research*, 40, 125, doi: [10.1134/S0038094606020067](https://doi.org/10.1134/S0038094606020067)
- Sylwester, B., Sylwester, J., Phillips, K. J. H., Kepa, A., & Mrozek, T. 2014, *ApJ*, 787, 122, doi: [10.1088/0004-637X/787/2/122](https://doi.org/10.1088/0004-637X/787/2/122)
- Vadawale, S. V., Shanmugam, M., Acharya, Y. B., et al. 2014, *Advances in Space Research*, 54, 2021, doi: [10.1016/j.asr.2013.06.002](https://doi.org/10.1016/j.asr.2013.06.002)
- Vadawale, S. V., Mithun, N. P. S., Mondal, B., et al. 2021, *ApJL*, 912, L13, doi: [10.3847/2041-8213/abf0b0](https://doi.org/10.3847/2041-8213/abf0b0)
- Warren, H. P. 2014, *ApJL*, 786, L2, doi: [10.1088/2041-8205/786/1/L2](https://doi.org/10.1088/2041-8205/786/1/L2)
- Warren, H. P., Mariska, J. T., & Doschek, G. A. 2013, *ApJ*, 770, 116, doi: [10.1088/0004-637X/770/2/116](https://doi.org/10.1088/0004-637X/770/2/116)